

# EXOSAT x-ray imaging optics

P. A. J. de Korte, R. Giralt, J. N. Coste, C. Ernu, S. Frindel, J. Flamand, and J. J. Contet

The European X-ray Observatory, EXOSAT, to be launched in 1981 will carry two Wolter I x-ray telescopes, each having a geometric area of  $\sim 100 \text{ cm}^2$ . A qualification model of the Wolter I optics has been manufactured and extensively tested in optical and x-ray beams. The influence of manufacturing tolerances on the resolution of the optics is discussed, and mechanical and optical measurements of those deviations are presented. Finally, the x-ray imaging quality of the optics is presented, and the correlation with the achieved tolerances is shown.

## I. Introduction

The European X-ray Observatory, EXOSAT, scheduled for launch in 1981 will carry as part of its scientific payload two high-resolution imaging telescopes for detailed spatial, spectral, and temporal studies of celestial x-ray sources. Each telescope system consists of a grazing incidence mirror in a Wolter I configuration with a geometric aperture of  $\sim 100 \text{ cm}^2$  and a set of focal plane detectors for image registration. The design goal for the grazing incidence optics was set at a resolution of 10 sec of arc half-energy width (HEW) for on-axis x rays. A qualification model of the grazing incidence optics has been manufactured and tested extensively. In the following sections we describe the critical parameters, the test results, and their correlation.

## II. The X-Ray Telescope and Its Production Method

The mirror assembly consists of a nested Wolter I configuration comprised of an inner and outer system. The paraboloids, hyperboloids, and field stops for the inner system are mounted onto a central structure. The field stops for the outer system are positioned on the

back of the inner system. The mirror assembly is illustrated in Fig. 1; the main physical characteristics are listed in Table I. Throughout this paper the outer paraboloid and hyperboloid will be called  $P1$  and  $H1$ , respectively, while those of the inner system are called  $P2$  and  $H2$ .

Due to the severe mass constraint of only 7 kg for the complete mirror assembly imposed by the spacecraft, an epoxy replica technique has been developed and used for the mirror fabrication. A detailed description of the manufacturing technique used to produce the glass master, the beryllium substrate, and the final replica mirror shells is given by Lainé *et al.*<sup>1</sup> For the purpose of this paper only a comprehensive description is given.

A master made out of BK7 glass (Schott, Germany) is polished to the shape accuracy and surface finish required for the reflecting surface of the mirror shells forming the assembly. A nonadherent gold layer ( $\approx 900 \text{ \AA}$ ) is evaporated onto the master. The mirror substrates are machined out of isopressed blocks of beryllium with an accuracy of several microns to ensure a uniform epoxy layer thickness. The replication process itself transfers the gold layer, evaporated on the master, onto the beryllium substrate by means of an intermediate epoxy layer of  $\sim 30 \text{ }\mu\text{m}$ . Experience has shown that the geometry<sup>1</sup> and surface finish<sup>2</sup> of the master can be transferred to the substrate without degradation.

We shall indicate the most obvious advantage of the replica technique over others, i.e., direct surfacing techniques in quartz, glass, and metal (Kanigen). The most costly part of x-ray optics manufacture is the polishing of the reflector surface. Experience with the replica method so far has shown that at least ten replicas can be made from one mandrel without impairing its surface quality. Therefore, to date the replica technique seems to be most promising for the realization of a LAMAR facility<sup>3,4</sup> consisting of Wolter I optics.

P. A. J. de Korte is with Cosmic Ray Working Group, Huygens Laboratory, Wassenaarseweg 78, 2300 RA Leiden, The Netherlands; R. Giralt is with European Space Agency, Space Science Department, European Space Research & Technology Centre, 2200 AG Noordwijk, The Netherlands; J. Flamand is with Jobin-Yvon, Instruments S.A. Division, Longjumeau, France; J. J. Contet is with Precision Optics J. Fichou, Fresnes, France; and the other authors are with CIT-ALCATEL, Department of Physics & Mechanics, Annecy, France.

Received 12 June 1980.

0003-6935/81/061080-09\$00.50/0.

© 1981 Optical Society of America.

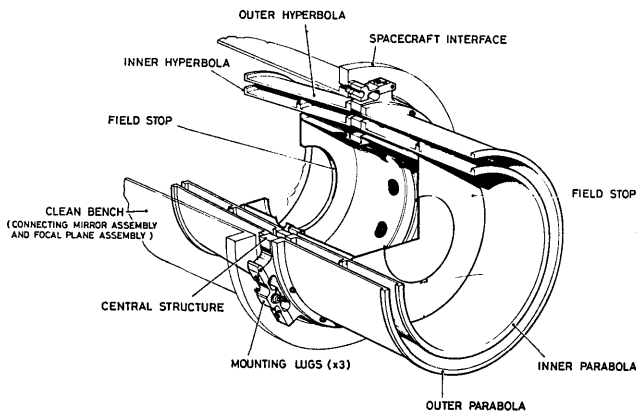


Fig. 1. Schematic of the EXOSAT mirror assembly.

Table I. General Characteristics of the EXOSAT Mirror Assembly

Designation	Inner mirror system	Outer mirror system
Entrance diameter	236 mm	278 mm
Length paraboloid/hyperboloid	200 mm	200 mm
Focal length	1090 mm	1090 mm
Average grazing angle	1°5	1°8
Geometric area	37.8 cm <sup>2</sup>	52.7 cm <sup>2</sup>
Reflective coating	gold	gold

### III. Quality Assessment and Final Calibration

At various stages of the manufacturing process specific measurement techniques are used to assess the quality of the product. They are discussed in some detail by Lainé *et al.*<sup>1</sup> A division can be made into three categories.

#### A. Mechanical Measurements

The most critical parameters to be measured on the master, substrate, and replicated mirror shells are the roundness and the profile. For the roundness measurements the technology to achieve the required accuracy ( $\sim 0.5 \mu\text{m}$ ) is directly available from a regular Talyrond. For the profile measurements, which require an accuracy of typically  $0.02 \mu\text{m}$  equivalent to 1 sec of arc over 4 mm, a special linear air bearing table has been constructed. An electrical induction gauge micrometer with a resolution of  $0.02 \mu\text{m}$  is mounted directly on the air bearing table, which is driven along the profile by a constant speed ac motor. The digitized gauge reading and the linear displacement of the table, given by a laser interferometer, are fed to a desk calculator. The deviation of the measured profile from the theoretical one is plotted vs the position along the profile. From this plot a slope error distribution of the profile is calculated by differentiation.

#### B. Optical Measurements

The critical parameters to be measured are the surface finish of the masters and replicated mirrors, the optical resolution (shape), and the focal length of the

individual mirror shells. Early in the program the use of a differential interference contrast microscope as a tool to investigate the surface roughness was evaluated.<sup>5</sup> Consequently, the polishing of the master is monitored with such a microscope. The microscope is also used to check the surface finish of the mirror shell directly after replication.

After replication each individual mirror shell is inspected optically in an autocollimation setup. The quality of the focus is evaluated by means of photographic recording and photoelectric analysis, i.e., slit and knife-edge scans. Also the focal length of each mirror shell is measured.

#### C. X-Ray Measurements

Pencil beam measurements in x rays are used to establish the reflectivity and scattering properties of each replicated individual mirror shell at the wavelengths of interest. The reflectivity is measured in an x-ray facility of the Space Research Laboratory at the University of Utrecht. For 100 points ( $1 \times 5\text{-mm}^2$  beam size), distributed uniformly over the mirror surface, the reflectivity has been measured at four wavelengths in the 8–67-Å range. The x-ray scattering properties were measured in a facility of the Cosmic Ray Working Group at the University of Leiden.<sup>2</sup> For 18 points on the mirror surface the scattering was measured at 8.3 Å, which is the shortest and therefore most critical wavelength at which the x-ray telescope will be used.

After the integration of the mirror assembly in an optical autocollimation facility,<sup>1</sup> an x-ray quality assessment of the integrated mirror assembly was carried out in the long beam facility (LBF) at Martin Marietta Aerospace, Denver, Colorado. A schematic layout of the facility is given in Fig. 2. It consists essentially of a 68-m long vacuum system with a source at one end and the mirror assembly mounted on a tilt-rotation table at the other end. The source size is defined by a 1-mm diam pinhole (equivalent to 3 sec of arc), irradiated by an x-ray gun or a hollow cathode UV source. With these two sources measurements have been carried out at six different wavelengths in the 7–300-Å range. Also an ordinary white lamp was used to carry out measurements in the visual wavelength band. The mirror assembly and the focal plane detector system are mounted on the tilt-rotation system, which enables measurements over a field of view of  $\sim 2^\circ$  diam. Since a position sensitive detector was not available to mea-

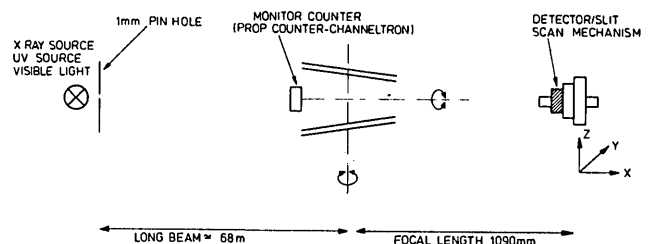


Fig. 2. Layout of the setup at the long beam facility.

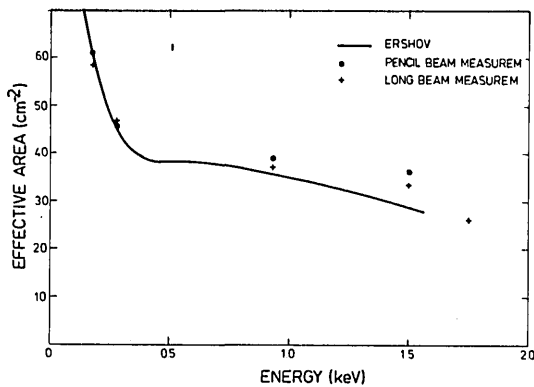


Fig. 3. Effective area as a function of x-ray energy derived from reflectivity values and measured at the long beam facility.

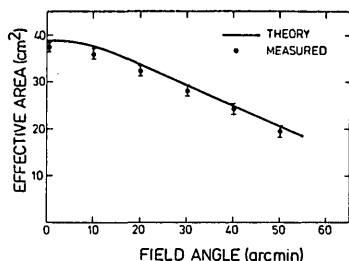


Fig. 4. Effective area at 0.94 keV (13.3 Å) as a function of field angle.

sure the intensity distribution in the image of the mirror assembly, a focal plane system consisting of three linear translators and a slit-masked detector was used. Two translators made it possible to scan the image in two directions, perpendicular to each other. The third one enabled us to change the position of the plane, into which the image is scanned, for depth of focus investigations. By remote control various slit masks could be placed in front of the detector. Three pairs of slits perpendicular to each other were available, i.e., 10, 50, and 250  $\mu\text{m}$ , equivalent to 2, 10, and 50 sec of arc, respectively. Also a totally open position was available in order to be able to measure the total image intensity simultaneously. To correct the measured image distribution for source intensity fluctuations during the scan a monitor detector was mounted in front of the inner field stop of the mirror assembly. Gas proportional detectors, channeltrons, and photometers were used for the measurements in the x-ray, UV, and visual domain, respectively. The detection efficiency of both gas proportional counters was calibrated to determine the absolute collecting area of the mirror assembly in the x-ray domain.

#### IV. Effective Area of the Mirror Assembly

The effective area of the mirror assembly is the product of the geometrical area and the reflection efficiencies for the paraboloid and hyperboloid. The geometrical area for the mirror assembly, given in Table I, equals 90.5  $\text{cm}^2$ , which consists of 37.8 and 52.7  $\text{cm}^2$  for the inner and outer system, respectively.

Reflectivity measurements on each individual shell were carried out with a pencil beam for 100 points distributed over the mirror surface. The reflectivity was measured at four different wavelengths, i.e., 67, 44, 13.3, and 8.3 Å, and at grazing incidence angles equal to that for radiation incident parallel to the optical axis of the mirror assembly, i.e., 1.84, 1.71, 1.56, and 1.46° for P1, H1, P2, and H2, respectively. These measurements show that the reflectivity is uniform over the mirror surface within a few percent. The effective area calculated, using these reflectivity values, is given in Fig. 3. The effective area calculated with the reflectivity values for gold given by Ershov *et al.*<sup>6</sup> and Lukirskii *et al.*<sup>7</sup> is also drawn. Comparison shows that the Ershov data yield a smaller effective area especially at the shorter wavelengths.

At the long beam test the effective area at the mirror assembly for on-axis radiation was measured for five different wavelengths. These values, corrected for 7.3% vignetting due to the finite source distance, are also shown in Fig. 3. They are in fair agreement with the values calculated from the reflectivity measurements carried out on the individual shells.

For one wavelength, i.e., 13.3 Å, the effective area was measured as a function of field angle. The results are given in Fig. 4. Also a calculated response is given, which has been calculated by a ray trace analysis, of the system with the reflectivities derived from Ershov's optical constants. The deviation of our reflectivity measurements from the Ershov data (Fig. 3) has a negligible influence on the shape of the calculated curve.

#### V. Imaging Quality

The on-axis quality is limited by the geometrical imperfections of the individual mirror shells and their alignment errors within the assembly.

##### A. Influence of Manufacturing Tolerances

For the mirror assembly the variety of possible geometrical aberrations can be specified by ten measurable errors, which are discussed in some detail by Vaiana *et al.*<sup>8</sup> and Hoover *et al.*<sup>9</sup> If the integration of the mirror assembly is carried out in an optical beam, most of these ten errors can become of minor importance if the mounting of the shells allows a few degrees of freedom: tilt errors between the optical axes of paraboloid and hyperboloid can be canceled by displacement of the paraboloid with respect to the hyperboloid perpendicular to the optical axis, and focal length differences between the inner and outer systems can be compensated by adjustment of the spacing between paraboloid and hyperboloid. In such a case the imaging quality is totally dominated by only a few geometrical aberrations of the individual mirror shells.

##### 1. Roundness

The mirror roundness is measured in several planes along the axis of the mirror shell. The deviation from roundness is composed of two components, i.e.,

(a) Roundness deviations with an equal phase at the

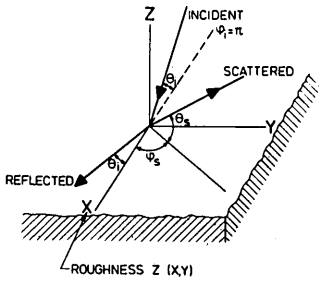


Fig. 5. Diagram of angles and the coordinate system.

entrance and exit plane of the mirror shell. Such an error results in a radial displacement of the mirror surface. The influence on the image quality in units of half-energy width (HEW) of the point spread function (PSF) equals  $\sim 2 \times 10^5 |\delta 1|/f$  sec of arc, with  $f$  the focal length of the mirror assembly, and  $\delta 1$  the maximum deviation from the average radius.

(b) Roundness deviations which are out of phase at the entrance and exit planes of the mirror shell. They represent slope errors of the mirror surface. The influence on the image quality (PSF) equals  $\sim 2 \times 10^5 |\delta 2|/L$  sec of arc (HEW).  $L$  is the length of the mirror shell, and  $\delta 2$  the maximum differential deviation from a circular radius at the entrance and exit planes.

## 2. Profile

Deviations from the nominal meridional profile represent slope errors of the mirror surface. Their influence on the image quality (PSF) is  $2\delta_3$  sec of arc HEW,  $\delta_3$  is equal to the full width at half-content of the slope error distribution of the profile. In order of decreasing scale length one can distinguish power errors, regularity errors, and surface roughness. The power error is a concave or convex deviation from the nominal profile. Regularity errors are undulations around the nominal profile with a scale length ranging from 0.5–0.1 of the profile length. The scale length is weakly correlated with the stroke length used for the polishing pad. Normally irregularities with a scale length shorter than those of the regularity errors are smoothed out by the polishing process. Therefore, the measurement accuracy needed to control the profile production is governed by the shortest regularity errors and the required angular accuracy.

On a much shorter scale length, this smoothing process breaks down due to a residual intrinsic surface roughness of the polished material. The influence of this surface roughness on the imaging quality can be estimated by the use of an x-ray scattering model.

## 3. Surface Roughness

The first-order vector perturbation scattering theory<sup>10–12</sup> provides a means to estimate the influence of surface roughness on the imaging quality of the telescope. In this paper we use the same notation as de Korte and Lainé.<sup>5</sup> The coordinate system and the angles are defined in Fig. 5. The differential scattered intensity is given by

$$\frac{dI}{d\Omega} = \frac{k^4}{\pi^2} \cdot I_i \cdot \sin\theta_i \cdot \sin^2\theta_s \cdot Q \cdot W(p, q), \quad (1)$$

where  $d\Omega = \cos\theta_s d\theta_s d\phi_s$ ;  $k = 2\pi/\lambda$ ;  $I_i$  is the total incident intensity;  $Q$  is the reflection efficiency in case of small scatter angles ( $\theta_s \rightarrow \theta_i$ ); and  $W(p, q)$  represents the two-dimensional power spectral density (2-D PSD) of the rough surface with

$$p = k\theta_i \alpha; \alpha = \theta_s - \theta_i, \quad q = k\phi_s, \quad (2)$$

approximations valid for small grazing incidence and scatter angles.

To estimate the influence of the surface roughness on the imaging quality we will assume that the surface can adequately be described by an exponential autocorrelation function

$$G(\tau) = \sigma^2 \exp(-\tau/\rho), \quad (3)$$

in which  $\sigma$  is the rms height of the rough surface,  $\rho$  the correlation length, and  $\tau$  the lag length on the surface. It is furthermore assumed that the surface roughness is isotropic. In that case, the 2-D PSD of the rough surface,  $W(p, q)$ , is equivalent to the Hankel transform of  $G(\tau)$ :

$$W(r) = 2\pi \int_0^\infty \tau G(\tau) J_0(r\tau) d\tau, \quad (4)$$

with  $J_0$  the zero-order Bessel function, and  $r^2 = p^2 + q^2$ . Replacement of  $G(\tau)$  by Eq. (3) gives

$$W(r) = \frac{2\pi\sigma^2\rho^2}{(1 + \rho^2 r^2)^{3/2}}. \quad (5)$$

So in the limit of small scatter angles,

$$\frac{dI}{d\Omega} = \frac{2k^4}{\pi} \cdot I_r \cdot \theta_i^3 \sigma^2 \rho^2 / [1 + \rho^2 k^2 (\alpha^2 \theta_i^2 + \phi_s^2)]^{3/2}, \quad (6)$$

with  $I_r$  the total reflected intensity. Integration of this equation over  $\phi_s$  gives

$$\frac{dI}{d\alpha} = \frac{4k^3}{\pi} \cdot \theta_i^3 \cdot I_r \cdot \frac{\sigma^2 \rho}{(1 + \rho^2 \theta_i^2 k^2 \alpha^2)}. \quad (7)$$

Equation (7) is valid for a planar geometry. In the case of a circular geometry such as a paraboloid or hyperboloid, the scattered distribution is described by a point spread function, which can be obtained by multiplying Eq. (7) with  $2/2\pi\alpha$ . Therefore,

$$\left(\frac{dI}{d\alpha}\right)_{\text{PSF}} = \frac{4k^3 \theta_i^3 \sigma^2 \rho I_r}{\pi^2 (\alpha + \rho^2 \theta_i^2 k^2 \alpha^3)}. \quad (8)$$

Integration over the differential scattered intensity gives

$$I_{sc} = 2\pi \int_0^\infty \alpha \left(\frac{dI}{d\alpha}\right)_{\text{PSF}} d\alpha = 4k^2 \theta_i^2 \sigma^2 \cdot I_r, \quad (9)$$

which is the well-known equation of the total scattered intensity in the limit of small scatter levels. The unapproximated equation equals

$$I_{sc} = \{1 - \exp[-(2k\theta_i\sigma)^2]\} I_r. \quad (10)$$

Since the scattering level of the EXOSAT mirror assembly at  $8.3 \text{ \AA}$  will turn out to be  $\sim 50\%$ , we will use Eq. (10) instead of Eq. (9) for the wavelength dependence

of the total scattered intensity  $I_{sc}$ . For the angular distribution we assume Eq. (8) to be still valid. We only rewrite it in order to make its integral intensity compliant with Eq. (10):

$$\left(\frac{dI}{d\alpha}\right)_{PSF} = \frac{\rho\theta_i k}{\pi^2(\alpha + \rho^2\theta_i^2 k^2 \alpha^3)} \cdot I_{sc}. \quad (11)$$

The way to add the influence of the manufacturing tolerances for paraboloid and hyperboloid is different for the three tolerances discussed so far. Roundness errors cannot be added. The flexibility present during mirror integration makes it possible to cancel the roundness errors of the paraboloid to a certain extent with the roundness errors of the hyperboloid. On the other hand, the fixation of the mirror shells onto the central structure might introduce additional roundness errors. Profile errors of both paraboloid and hyperboloid are assumed to be rather random so that they can be added quadratically. In first-order approximation the scattering of the paraboloid and hyperboloid can be added linearly, neglecting double scattering.

### B. Characteristics of the Individual Mirror Shells

On the final mirror shells a complete set of mechanical measurements has been carried out in order to establish to which extent the specified tolerances were met. The measurement results are given in Table II. From complementary measurements on both the masters and Be substrates one can trace the origin of the various errors. The profile errors are to the largest extent caused by the imperfections of the master, since the replica profiles are true copies. As an example, the deviations from the nominal profile for both the P1 master and P1 replica mirrors are given in Fig. 6. On the other hand the roundness errors are due mainly to roundness errors of the Be substrates, which are propagated onto the replica mirrors by the replica process. In Table II the resolution (HEW) derived from the mechanical measurements is also given. For this purpose the influence of the roundness and profile errors has been added quadratically.

Each mirror was tested optically in an autocollimation setup. The asymmetry observed in the point spread functions of the mirror shells corresponds very well with the deviations from roundness given in Table II. The resolution (HEW) of the line spread function (LSF) measured in the autocollimation setup is given in Table III. To compare these figures with the resolutions derived from the mechanical measurement one must transfer the optically measured values to a PSF. The ratio of the HEW for a PSF and a LSF varies between 1.73 and 1.8 for optics with an exponential or Gaussian modulation transfer function, respectively. Since the distribution measured for the line spread function is compatible with an exponential MTF, we apply a factor of 1.73. Since the measurements are carried out in autocollimation, the geometry errors propagate twice. Therefore, the image quality measured in autocollimation is expected to be worse by a factor of between  $\sqrt{2}$  and 2 than that measured in a parallel beam facility. The factor  $\sqrt{2}$  will apply to the

Table II. Mechanical Aberrations of the Mirror Shells

Designation	P1	P2	H1	H2	Design goal
Roundness deviations					
in phase ( $\mu\text{m}$ ):	2.4	1.5	2.5	1.3	2.5
out of phase ( $\mu\text{m}$ ):	3.6	3.0	6.5	4.2	1.0
Profile deviations					
rms ( $\mu\text{m}$ ):	0.36	0.22	0.40	0.20	
50% width (sec of arc):	5	7	4	5	2.5
Expected PSF resolution (sec of arc HEW):	10.6	14.3	10.3	10.8	5.1

Table III. Optical Characteristics of the Mirror Shells

Designation	P1	P2	H1	H2
Resolution <sup>a</sup> (HEW) of the LSF (sec of arc)	9.2	11.3	8.5	9.5
Resolution (HEW) min. of the PSF (sec of arc) max.	8.0	9.8	7.4	8.3
	11.3	13.8	10.4	11.6

<sup>a</sup> Measured in autocollimation.

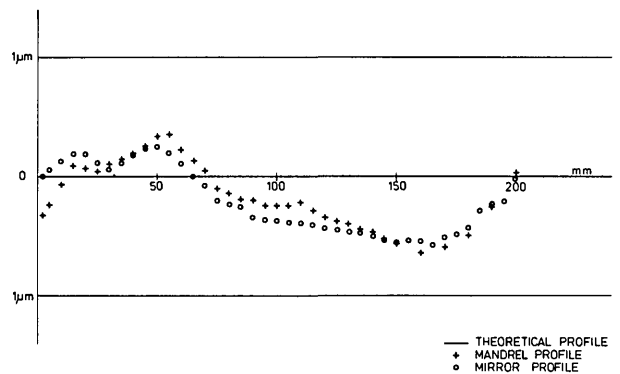


Fig. 6. Mechanical profile measurements for the P1 master and its replica.

short scale errors, such as, for example, the smaller profile errors, while the factor of 2 will hold for long scale errors as roundness deviations. So the resolution (HEW) of the LSF (Table III) can be transferred to a value for the PSF by multiplication with a factor between  $1.73/\sqrt{2}$  and  $1.73/2$ . Both values are also given in Table III.

That the profile errors contribute to their full extent to the optical image quality is questionable, since they will be partly below the diffraction limit. For short scale length fluctuations the Strehl criterium of 0.8 for a diffraction-limited imaging device corresponds to rms wave front errors equal to  $\lambda/14$ .<sup>13</sup> The rms profile errors are between 0.2 and 0.4  $\mu\text{m}$  for the various shells (Table II), which corresponds to wave front errors (in autocollimation) of between  $\lambda/17$  and  $\lambda/35$ . It is, therefore, not surprising that the measured optical image resolution (HEW) tends to be a bit better than the values derived from the mechanical measurements.

X-ray scattering measurements have been carried out on the individual mirror shells in a pencil beam facility at 8.3 Å and at grazing incidence angles which correspond to on-axis illumination of the mirror assembly, i.e., between 1.46 and 1.84°. Due to measurement constraints, the scattering has only to be determined for scatter angles between 1 and 12 min of arc. The scatter levels measured between these scatter angles equal 16.3, 1.6, 9.9, and 20.4% of the total reflected intensity for P1, H1, P2, and H2, respectively. On the basis of these measurements one expects a scatter level (8.3 Å, 1–12 min of arc) of 17.6, 28.3, and 22.5% for the outer, inner, and total mirror assemblies, respectively. It must be mentioned that the scatter levels measured on the four replica mirror shells correlate rather well with the surface roughness of the masters as observed with the Nomarski interference contrast microscope.

### C. Characteristics of the Mirror Assembly

To obtain an optimum imaging quality, the integration of the mirror assembly was carried out in an auto-collimation setup. This enables us to measure the image quality during all stages of the integration. The large degree of freedom for the selection of the rotational position of the paraboloids with respect to the hyperboloids allows us to obtain a maximum cancellation of shape errors on paraboloid and hyperboloid. The best resolution of the LSF, measured in autocollimation, equals 9.5-sec of arc HEW, which is about equal to the average quality of the individual mirror shells. This quality could, however, only be obtained with freestanding mirror shells. The fixation of the mirror shells to the central structure introduced additional roundness deviations. The best image quality, which could be achieved for the fixed mirror assembly, varies between 11.0- and 13.3-sec of arc HEW (LSF, autocollimation), depending on the scan direction over the image. In this configuration the mirror assembly underwent a final calibration at the long beam facility (LBF) at Martin Marietta.

At the LBF, imaging quality measurements were carried out at visual, XUV, and x-ray wavelengths. First, measurements were carried out on the on-axis imaging quality as a function of focal plane position. The results for the visual wavelength band as well as for C-K $\alpha$  (44 Å) and Al-K $\alpha$  (8.3 Å) are given in Fig. 7. Two types of data are presented, i.e., the peak intensity of the LSF (integrated in a 10- $\mu$ m wide slit) and the FWHM of the LSF. The results of both methods are in fair agreement and wavelength independent. In the optimum focal plane position, the zero position in Fig. 7, the line spread function was measured to great accuracy in two directions perpendicular to each other, i.e., Y and Z. Two typical examples of such a LSF, i.e., for C-K $\alpha$  (44 Å) and Al-K $\alpha$  (8.3 Å), are given in Fig. 8.

Since the flight instrument will have 2-D position sensitive detectors, we decided to calculate the PSF from the measured LSF by means of the Abell transform.<sup>14</sup> For this purpose the LSF measured in the Y and Z directions, which are almost identical, has been averaged. In Fig. 9 the central part of the PSF is given

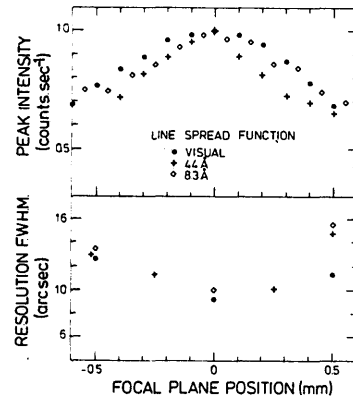


Fig. 7. Image quality vs focal plane position for visual and x-ray wavelengths.

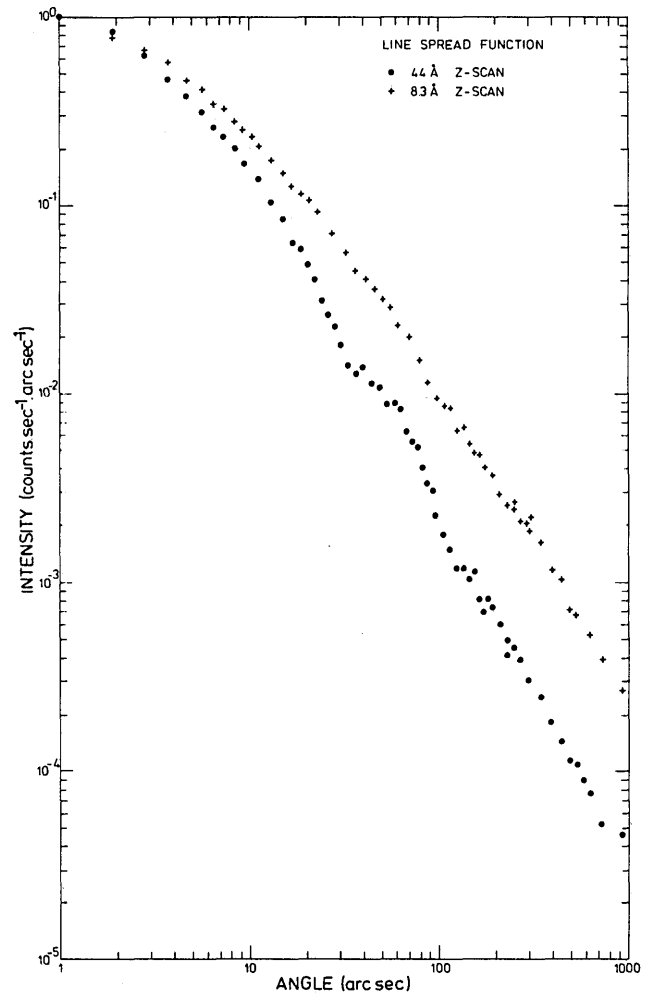


Fig. 8. Line spread function (Z scan) for 44 and 8.3 Å.

for two x-ray wavelengths, i.e., 44 and 8.3 Å. Both distributions have a FWHM of  $\sim 5$  sec of arc. The flattop of the distribution ( $\sim 2$  sec of arc) is due to the finite size of the x-ray source (3 sec of arc). From these two distributions it is apparent that the central part of the PSF is unaffected by x-ray scattering.

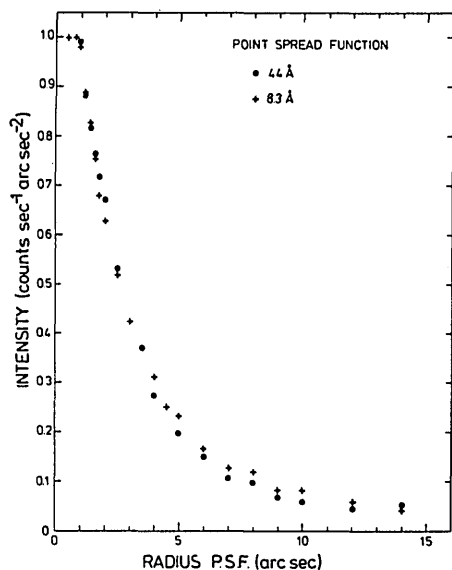


Fig. 9. Central part of the point spread function at 44, 13.3, and 8.3 Å.

Table IV. PSF Resolution (HEW) for the Mirror Assembly (sec of arc)

Visual wavelength band		X rays (Å)			
A <sup>a</sup>	B <sup>b</sup>	304	44	13.3	8.3
10.5-15	16	19	19	27	39

<sup>a</sup> Measured with the autocollimation alignment setup. The two values refer to the factor of  $\sqrt{2}$  or 2.

<sup>b</sup> Measured at the long beam facility prior to the x-ray measurements.

The HEW, however, is strongly affected by x-ray scattering and is, therefore, a better quantity to define the image quality of an x-ray telescope. The HEW of the PSF obtained for various wavelengths is given in Table IV. A few things are apparent from the data given in this table. First, the image quality measured in the visual wavelength bands is better than that measured at the longer x-ray wavelengths. This is almost certainly due to the fact that part of the profile errors are below the diffraction limit at optical wavelengths. The fact that the optical resolution measured in the alignment autocollimation setup (A) is better than that measured at the LBF (B) is most probably due to air turbulence in the 68-m long guide tube at the LBF. The resolution expected from the mechanical measured profile errors (Table II) equals 15 sec of arc. This, together with the influence of the roundness errors introduced by the fixation of the mirror shells onto the central structure, might account for the total of 19-sec of arc HEW measured at the longer x-ray wavelengths. Second, the scattering only starts to become important at wavelengths shorter than 44 Å, since the image quality at 304 and 44 Å is identical. The influence of the x-ray scattering on the image quality is shown on detail in Figs. 10 and 11. The PSF measured out to

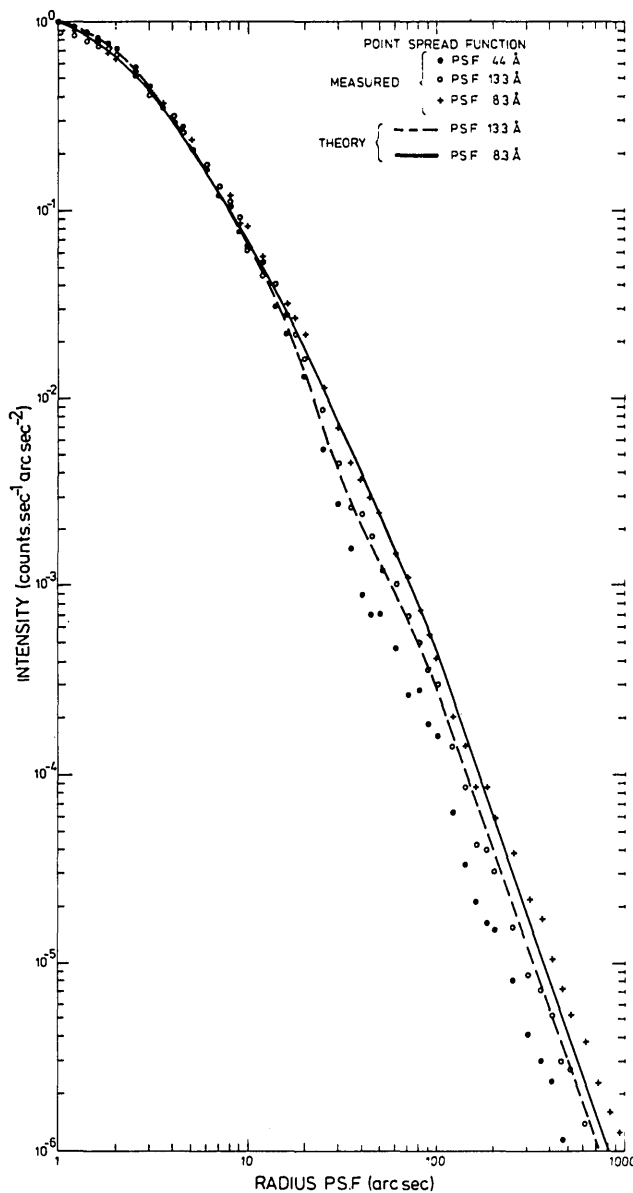


Fig. 10. Point spread function of the mirror assembly for 44, 13.3, and 8.3 Å.

1000 sec of arc is given in Fig. 10 for 8.3, 13.3, and 44 Å. They all are normalized onto the peak intensity of the distribution. In Fig. 11 the fractional area of the telescope as a function of image radius is given for the three x-ray wavelengths. These three curves are normalized onto the fractional area at 1000 sec of arc. The distributions for 304 Å are not given since they are identical to the ones at 44 Å. This again demonstrates that the influence of x-ray scattering only starts to become important for wavelengths shorter than 44 Å.

In addition to data points, Figs. 10 and 11 also contain predictions based on the scatter theory. The theoretical curves have been derived in the following way. The PSFs at 13.3 and 8.3 Å are assumed to be made up of two components, i.e., a scattered component having the intensity distribution given by Eqs. (11) and a specular

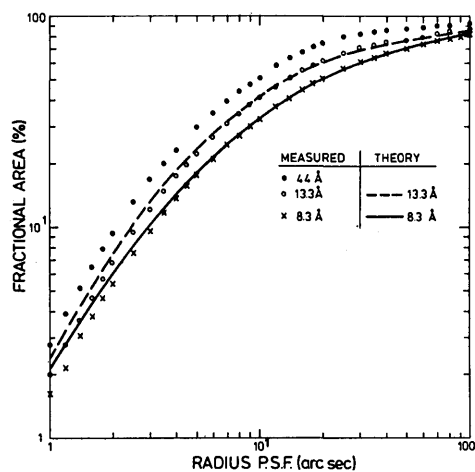


Fig. 11. Fractional area vs the radius over which the point spread function is integrated for 44, 13.3, and 8.3 Å.

reflected intensity distribution that is identical to the one measured at 304 and 44 Å. The total intensity of the scattered radiation is assumed to obey Eq. (10). Therefore, two free parameters are actually left, i.e., the correlation length  $\rho$  and surface roughness rms height  $\sigma$ . These two parameters can be obtained by making a fit to the HEW resolution measured at 44, 13.3, and 8.3 Å. An excellent fit is obtained for  $\rho = 20 \mu\text{m}$  and  $\sigma = 19 \text{Å}$ , which is equivalent to a total scattered intensity of 50, 23.7, and 2% at 8.3, 13.3, and 44 Å, respectively. That such a fit does not only explain the HEW is shown in Figs. 10 and 11. It is really surprising to see that such a simple surface roughness model already leads to a very good agreement between the measured and predicted PSF.

Another important point to be mentioned is that the x-ray intensity of the point spread function between 1 and 12 min of arc, i.e., 22%, is almost exactly equal to the level expected from the x-ray scattering measurements on the individual mirror shells (22.5%). So pencil beam measurements on individual mirror shells give an excellent indication of the scatter levels to be expected for the integrated mirror assembly.

Image quality measurements have also been carried out in the field of optics up to 40-min of arc off-axis. Both sagittal and meridional LSFs have been measured for both 44 and 8.3 Å. Since the measured resolution (FWHM) for the various measurements is essential independent of wavelength, we have given the average values in Fig. 12. Also the results to be expected for an error free mirror are indicated. These values have been calculated with a ray trace program. For off-axis angles larger than 10 min of arc, the measurements are in reasonable agreement with the calculations.

## VI. Discussion

Results have been given on the performance of the qualification model of the EXOSAT Wolter I replica mirror assembly. It is shown that the influence of the two most important aberrations, i.e., roundness and profile deviations, on the image quality is in agreement with theoretical expectations. The resolution (HEW)

measured at visual wavelengths is somewhat better than expected from the mechanical roundness and profile measurements. This is certainly due to the fact that part of the profile deviations is below the diffraction limit. The resolution measured at the longer x-ray wavelengths complies quite well with the mechanical expectations. So, to produce a good x-ray mirror, a highly accurate ( $\approx 0.02\text{-}\mu\text{m}$ ) profile measurement device is essential.

At shorter x-ray wavelengths, x-ray scattering becomes important. The scatter levels measured in the long beam facility agree with those measured on the individual mirror shells in a pencil beam facility. Also the roughness of the surfaces seen by means of the Nomarski interference contrast microscope complies with these observations. It is shown that a simple surface roughness model, i.e., an exponential autocorrelation function, can explain the x-ray measurements. The major importance of such a model is the possibility to estimate the influence of surface roughness on the image quality. This gives a tool to tolerance the surface roughness for future telescope programs.

The x-ray reflectivities of the individual mirror shells measured with a pencil beam turn out to be in fair agreement with the measured effective area of the mirror assembly. At present, October 1980, all flight model mirror shells have been produced. Before their production the profile deviations of the four masters were improved to a 50% angular width ( $\delta\theta$ ) of 2.5 sec of arc. Also their surface roughness was drastically improved.

Mechanical measurements of all the replicated flight model mirror shells give a 50% angular width of the profile of 3 sec of arc. This is an improvement of  $\sim 75\%$  over the mirror discussed in this paper. X-ray pencil beam measurements on all eight flight model mirror shells give x-ray scattering levels smaller than 3% for each shell at 8.3 Å and between 1 and 12 min of arc. This is an improvement by a factor of 3–4 with respect to the mirror discussed in this paper. On the basis of the correlation between x-ray quality and all kind of other verification techniques discussed in this paper,

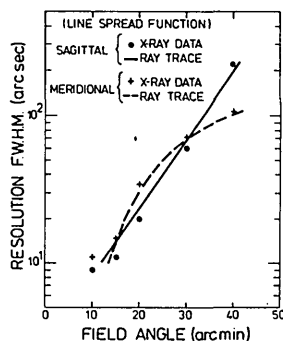


Fig. 12. Resolution of the LSF (FWHM) for the mirror assembly as a function of field angle.

one can predict that the EXOSAT flight model optics will have a PSF quality equal to 10–15-sec of arc HEW at 8.3 Å.

How does the x-ray performance discussed in this paper compare with that of x-ray optics produced in other programs? In the field of replica x-ray optics the present development is unique, although one other publication is known to us.<sup>15</sup> In the field of metal optics it can be compared with the S-54 telescope on Skylab,<sup>16</sup> the 32-cm telescope of the Max-Planck Institute,<sup>17</sup> and several telescopes produced by single diamond turning.<sup>18,19</sup> Of all these telescopes, x-ray data or indication of x-ray resolution exist only for the S-54<sup>16</sup> and the Wolter-Schwarzschild optics of Berkeley.<sup>18</sup> For the S-54, 96-sec of arc HEW at 7 Å and for the Berkeley telescope ~15-sec of arc FWHM vs 39-sec of arc HEW at 8.3 Å and 5-sec of arc FWHM for the telescope described in this paper.

A proper comparison can be made with the quartz optics onboard the Einstein Observatory.<sup>20</sup> They have a quality (PSF) of 4-sec of arc FWHM and 11-sec of arc HEW at 8.3 Å, which must be compared with 5 and 39 sec of arc, respectively.

In conclusion it can be said that the telescope described in this paper is of a better quality than all the x-ray optics reported so far, except for the quartz telescope onboard the Einstein Observatory. It is plausible that the flight model optics of the EXOSAT mission will have x-ray imaging properties comparable with that of the Einstein mission. That is to say, replica optics can obtain a quality equal to that obtained in a glass technology, and it is appreciably better than the results obtained so far in other metal technologies.

The authors wish to express their thanks to E. Röss, J. Froechtenigt, and W. Miles of Martin Marietta Corp. for their continuous efforts at the Long Beam Facility. We are also grateful to F. A. van Rooyen and A. Naber of the Space Research Laboratory at the University of Utrecht and L. de Jong of the Cosmic Ray Working Group at the University of Leiden for their assistance with the x-ray measurements. R. Zobl and B. G. Taylor of the European Space Agency are acknowledged for supporting the program. One of us (P. de Korte) wants to thank J. A. M. Bleeker for the stimulating discussions.

The work reported here forms part of and was supported by the program for development of the scientific payload for the European Space Agency's x-ray astronomy satellite, EXOSAT.

## References

1. R. Lainé, R. Giralt, R. Zobl, P. A. J. de Korte, and J. A. M. Bleeker, *Proc. Soc. Photo-Opt. Instrum. Eng.* **184**, 181 (1979).
2. P. A. J. de Korte, *Proc. Soc. Photo-Opt. Instrum. Eng.* **184**, 189 (1979).
3. P. Gorenstein, *Proc. Soc. Photo-Opt. Instrum. Eng.* **184**, 63 (1979).
4. R. C. Catura, W. A. Brown, and L. W. Acton, *Opt. Eng.* **19**, 602 (1980).
5. P. A. J. de Korte and R. Lainé, *Appl. Opt.* **18**, 236 (1979).
6. O. A. Ershov, I. A. Brytov, and A. P. Lukirskii, *Opt. Spectrosc. USSR* **22**, 66 (1967).
7. A. P. Lukirskii, E. P. Savinov, O. A. Ershov, and Y. F. Shepelev, *Opt. Spectrosc. USSR* **16**, 168 (1964).
8. G. S. Vaiana, A. S. Krieger, R. Petrasso, J. K. Silk, and A. F. Timothy, presented at the Seminar on Instrumentation in Astronomy, Tucson, Arizona (1974).
9. R. B. Hoover, R. J. Thomas, and J. H. Underwood, *Adv. Space Sci. Technol.* **11**, 1 (1972).
10. E. L. Church and J. M. Zavada, *Appl. Opt.* **14**, 1788 (1975).
11. E. L. Church, H. A. Jenkinson, and J. M. Zavada, *Opt. Eng.* **16**, 360 (1977).
12. J. M. Elson and J. M. Bennett, *J. Opt. Soc. Am.* **69**, 31 (1979).
13. M. Born and E. Wolf, *Principles of Optics* (Pergamon, London, 1964), see Diffraction Theory of Aberrations.
14. R. M. Bracewell, *Fourier Transform and Its Application* (McGraw-Hill, New York, 1965).
15. W. R. Hunter, D. J. Michels, C. M. Fleetwood, J. D. Mangus, and B. W. Bach, *Appl. Opt.* **19**, 2128 (1980).
16. G. S. Vaiana, L. P. VanSpeybroeck, M. V. Zombeck, A. S. Krieger, J. K. Silk, and A. Timothy, *Space Sci. Instrum.* **3**, 19 (1977).
17. J. Trümper, B. Aschenbach, and J. Bräumiger, *Proc. Soc. Photo-Opt. Instrum. Eng.* **184**, 12 (1979).
18. R. F. Malina, S. Bowyer, D. Finley, and W. Cash, *Opt. Eng.* **19**, 211 (1980).
19. R. C. Catura, L. W. Acton, R. Berthelsdorf, P. W. Sanford, A. Frank, *Proc. Soc. Photo-Opt. Instrum. Eng.* **184**, 23 (1979).
20. L. P. VanSpeybroeck, *Proc. Soc. Photo-Opt. Instrum. Eng.* **184**, 2 (1979).